Chinese Journal of
POLYMER SCIENCE

RESEARCH ARTICLE

https://doi.org/10.1007/s10118-023-3059-3
Chinese J. Polym. Sci. **2024**, *42*, 299–310

Production of Functional Materials Derived from Regenerated Silk Fibroin by Utilizing 3D Printing and Biomimetic Enzyme-induced Mineralization

Ni Chen, Fei-Yu Luo, Gong-Wen Yang, Jin-Rong Yao, Xin Chen, and Zheng-Zhong Shao*

State Key Laboratory of Molecular Engineering of Polymers, Laboratory of Advanced Materials and Department of Macromolecular Science, Fudan University, Shanghai 200433, China

Electronic Supplementary Information

Abstract Critical-sized bone defects, commonly encountered in clinical orthopedic surgery, present a significant challenge. One of the promising solutions is to prepare synthetic bone substitute materials with precise structural control, mechanical compatibility, and enhanced osteogenic induction performance, nevertheless the successful preparation of such materials remains difficult. In this study, a two-step technique, integrating an extrusion-based printing process with biomimetic mineralization induced by alkaline phosphatase (ALP), was developed. Initially, a pre-cured hydrogel of regenerated silk fibroin (RSF) with a small quantity of hydroxypropyl cellulose (HPC) and ALP was prepared through heating the mixed aqueous solution. This pre-cured hydrogel demonstrated thixotropic property and could be directly extruded into predetermined structures through a 3D-printer. Subsequently, the 3D-printed RSF-based materials with ALP underwent biomimetic *in situ* mineralization in calcium glycerophosphate (Ca-GP) mineralizing solution, utilizing the polymer chains of RSF as templates and ALP as a trigger for cleaving phosphate bonds of Ca-GP. The resulting 3D-printed RSF-mineral composites including hydrogel and sponge possessed adjustable compression modulus of megapascal grade and variable hydroxyapatite content, which could be controlled by manipulating the duration of the mineralization process. Moreover, these 3D-printed RSF-mineral composites demonstrated non-cytotoxicity towards rat bone marrow mesenchymal stem cells. Therefore, they may hold great potential for applications involving the replacement of tissues characterized by osteoinductivity and intricate structures.

Keywords Silk protein; Alkaline phosphatase; Extrusion-based printing; Biomineralization

Citation: Chen, N.; Luo, F. Y.; Yang, G. W.; Yao, J. R.; Chen, X.; Shao, Z. Z. Production of functional materials derived from regenerated silk fibroin by utilizing 3D printing and biomimetic enzyme-induced mineralization. *Chinese J. Polym. Sci.* **2024**, *42*, 299–310.

INTRODUCTION

The treatment of critical-sized bone defects presents a significant challenge within the field of clinical orthopedic surgery.[1–3] Current strategies for addressing this issue encompass autografts, allografts, and synthetic bone substitute materials.[4] However, both autografts and allografts exhibit inherent limitations, such as restricted donor sites, donor lesions, immune rejection and suboptimal biomechanical properties.[2,5] Conversely, synthetic bone substitute materials hold considerable promise for clinical development. Nonetheless, the preparation of durable synthetic bone substitute materials that meet the applicational requirements remains a challenge, particularly when considering factors such as mechanical strength, modulus matching, and osteogenic induction properties. Furthermore, these synthetic bone substitute materials ideally should possess enhanced biofunctionality to replicate micro and nano-scale topographical and biofactor cues found in the extracellular environment.[6,7]

Within the realm of synthetic bone substitute materials, a number of researches have been focusing on polymer-based composites doped with hydroxyapatite (HAP).[8–10] The appeal of HAP lies in its chemical structure and physical properties, which closely resemble those of natural bone mineral, and its remarkable osteoinductive capabilities.[11] Additionally, the polymer matrix within the composite improves the brittleness commonly associated with conventional hydroxyapatite-based bone cement materials, while also serves as a temporary extracellular matrix for bone tissue healing.[12] Therefore, polymer-based composites doped with HAP could be very promising bone substitute materials. Polymer matrices involved in osteoinductive materials can be categorized into two types: synthetic polymers, such as polycaprolactone (PCL) and polylactic acid (PLA), offering advantages in terms of high mechanical strength and structural stability but lacking of biocompatibility or biofunctionality;[13,14] or natural

* Corresponding author, E-mail: zzshao@fudan.edu.cn
Received August 23, 2023; Accepted October 12, 2023; Published online November 15, 2023

polymers, such as sodium alginate (SA) and gelatin, which typically exhibit biocompatibility and biodegradability but have dissatisfying mechanical properties.[15,16] Surprisingly, regenerated silk fibroin (RSF), extracted from *Bombyx mori* silk fiber, not only exhibits favorable biocompatibility[17] but also possesses excellent mechanical properties that rival those of synthetic polymers, which are achieved through the regulation of size, density, and distribution of β-sheet.[18] These β-sheet domains are commonly regarded as the source of high mechanical strength in RSF-based materials.[19] Given its biocompatibility and potential for excellent mechanical properties, RSF holds significant potential as a matrix material for bone implantation. Based on the mentioned above, the RSF and HAP composite materials may be regarded as an ideal biomaterial for bone repair.

However, the preparation of an ideal composite material consisting of RSF and HAP presents a formidable challenge due to the tendency of HAP to agglomerate in RSF aqueous solution. To achieve homogeneous RSF and HAP composites, various approaches have been explored. For instance, Kim *et al*.[20] enhanced the dispersion of HAP in an aqueous solution by grafting γ-glycidoxypropyltrimethoxysilane onto its surface, leading to improved dispersion when the HAP content was below 20 wt%. Our research group also endeavored to obtain homogeneous RSF and HAP composites through several methods. Mi *et al*.[21] employed RSF to modulate the growth and crystallization of calcium phosphate, resulting in an RSF nanofibril/HAP injectable hydrogel. However, achieving a HAP-content exceeding 20 wt% in the composite proved challenging. Subsequently, Yan *et al*.[22] synthesized HAP-RSF core-shell nanoparticles using a co-precipitation technique. Although this technique enabled the production of a homogeneous RSF/HAP-RSF bulk material with HAP content of 30 wt%, the procedures involved inherent complexity. Thus, even though all these attempts above improved the dispersion of HAP in RSF aqueous solution to some extent and yielded homogeneous RSF and HAP composites, they suffered from disadvantages such as low HAP content, laborious preparation procedures, and plain structures of the composites.

Inspired by diverse physiological processes in living organisms, researchers have sought to incorporate bioactive components into materials to confer them with living features.[23–25] In particular, alkaline phosphatase (ALP)-involved biomimetic mineralization, involves utilizing non-living polymer backbones as templates for biomineralization, yielding composites that mimic or surpass their natural counterparts with the assistance of the enzyme. To be specific, ALP is capable of rapidly cleaving phosphate bonds of alcohols, amines, pyrophosphates, and phenols with high specificity and high efficiency.[26] It has been proved that the phosphate ions, cleaved from calcium glycerophosphate (Ca-GP) through the catalytic action of alkaline phosphatase (ALP), could readily associate with dissociated calcium ions, culminating in the formation of calcium-phosphate salts.[27–29] This process further facilitates *in situ* biomineralization within ALP-involved polymer hydrogels when submerged in a Ca-GP mineralizing solution, resulting in the mineral content of the ALP-involved polymer hydrogels reaching to 45 wt% or even more. Nonetheless, concerns arose regarding the potential limited penetration of mineralization into the bulk hydrogel, resulting in surface-limited mineralization.

The extrusion-based printing technique has the capability to produce micro-scale porous structures, which exhibits a significantly larger specific surface area compared to an equal volume of bulk material.[30] Incorporating ALP into 3D-printed materials not only enhances the efficiency of *in situ* mineralization process facilitated by ALP but also enables to provide more intricate structures that may replicate the natural tissue structure and composition. Hence, the combination of 3D-printing technology and enzyme-induced biomimetic mineralization represents a promising strategy for the development of novel bone substitute materials.

In this study, we expect to fabricate a novel RSF and HAP composite material with mechanical compatibility, higher HAP content, and a more intricate structure. This aim will be accomplished by combining the preparation of an ALP-involved RSF pre-cured hydrogel with thixotropic properties and an enzyme-induced biomimetic mineralization process caused by ALP. The resulting pre-cured hydrogel can be extruded directly by a 3D-printer to achieve a predetermined structure, thereby facilitating the production of uniform 3D-printed RSF-HAP composite material *via* ALP-mediated biomimetic mineralization in a Ca-GP mineralizing solution. The preparation procedures were schemed as Fig. 1. To investigate the relationship between the microstructure of the pre-cured hydrogel and its thixotropic behavior, rheological tests on the pre-cured hydrogels were conducted and the microscopic morphology of lyophilized samples at various gelation stages was observed. Subsequently, the 3D-printed RSF-based materials, specifically 3D-printed pre-cured hydrogel and 3D-printed sponge, were obtained through the 3D-printing process followed by lyophilization. After biomimetic mineralization, the microstructure, mechanical properties, and cytotoxicity of the resulting 3D-printed RSF-mineral composites (both hydrogel and sponge) were assessed to preliminarily evaluate their suitability for bone tissue engineering applications.

EXPERIMENTAL

Materials

Mulberry cocoons were sourced from Jiangsu Province, China. Alkaline phosphatase (≥10 DEA units/mg solid) and hydroxypropyl cellulose (M_w: ~10 kDa; viscosity: 65–175 cP, 5 wt% in H_2O, 25 °C) were procured from Sigma-Aldrich. Calcium glycerophosphate was obtained from TCI (Shanghai) Chemical Industry Development Co. Ltd. The dialysis bags (the cut-off molecular weight: 12–14 kDa) were acquired from Shanghai Greenbird Technology Development Co.

The RSF aqueous solution was prepared following our previously established method,[31] which involved three distinct processes: degumming, dissolution, and concentration. Initially, 40 g of clean mulberry cocoons were boiled in 0.5 wt% Na_2CO_3 aqueous solution for 45 min to remove sericin from the surface of silk fibers. After three rinses with deionized water, the degummed silk fibers were dried overnight at 40 °C in an oven. Subsequently, the degummed silk fibers were dissolved in a 9.3 mol/L LiBr aqueous solution at 60°C for 1 h. The

https://doi.org/10.1007/s10118-023-3059-3

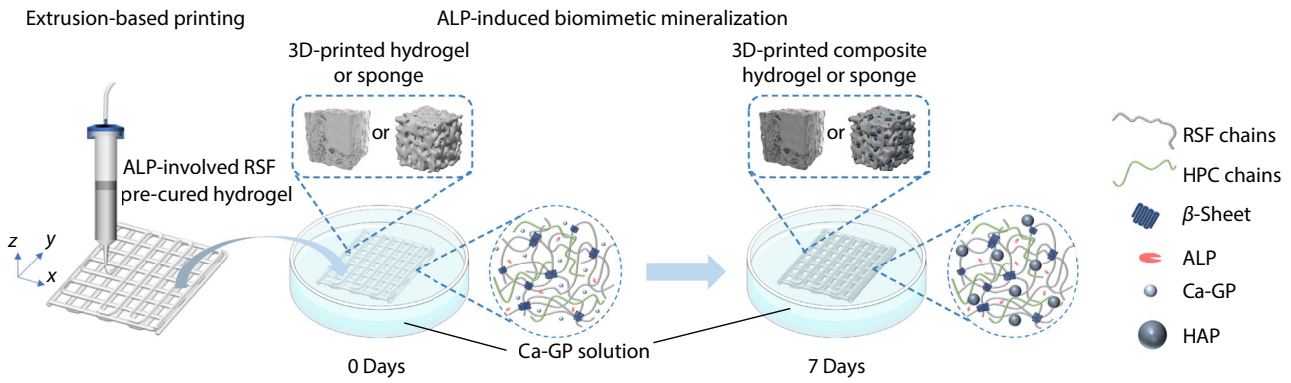

Fig. 1 ALP-induced biomimetic mineralization of 3D-printed hydrogel or sponge derived from RSF. ALP: alkaline phosphatase; RSF: regenerated silk fibroin; HPC: hydroxypropyl cellulose; Ca-GP: calcium glycerophosphate; HAP: hydroxyapatite.

resulting solution underwent filtration through eight layers of gauze to eliminate insoluble impurities and was then dialyzed against deionized water for 3 days. Following dialysis, the RSF aqueous solution underwent successive centrifugation (8000 r/min, 10 min) and filtration through eight layers of gauze, resulting in a fresh RSF aqueous solution with a mass fraction of approximately 4 wt%. Concentration of the fresh RSF aqueous solution was achieved through reverse dialysis using a PEG aqueous solution, with the final concentration determined by weighing method before storage in a refrigerator at 4 °C. Additionally, the HPC powder was dissolved in deionized water while magnetically stirred, yielding a 10 wt% HPC aqueous solution, which was also stored in a refrigerator at 4 °C.

Preparation of Pre-cured Hydrogels

To prepare the RSF pre-cured hydrogels, a mixed aqueous solution comprising RSF and HPC was formulated with a solid content of 20 wt%. The mass ratio of RSF to HPC in the formulation was set as 8:2, and the resulting mixed aqueous solution was designated as s-0. By diluting the 20 wt% mixed aqueous solution, aqueous solutions with solid contents of 10 wt% and 15 wt% were obtained. These varied aqueous solutions were then heated in a water bath at 38 °C for 6 h, resulting in the formation of pre-cured hydrogels. The resulting hydrogels were named pre-cured hydrogel-10, pre-cured hydrogel-15, and pre-cured hydrogel-20, indicating their respective solid contents.

Furthermore, to prepare the ALP-involved pre-cured hydrogels of RSF, aqueous solutions containing RSF, HPC, and ALP were prepared with a solid content of 20 wt%. The mass ratio of RSF to HPC was set at 8:2, and the mass of ALP accounted for 0.2 wt%, 0.4 wt%, and 0.6 wt% of the total mass of the mixed solutions. These solutions were named as s-0.2, s-0.4, and s-0.6, respectively. After undergoing a 6-h heating process at 38 °C, the corresponding ALP-involved pre-cured hydrogels were obtained and labeled as pre-cured hydrogel-0.2, pre-cured hydrogel-0.4, and pre-cured hydrogel-0.6.

Rheological Measurements

The rheological assessments were conducted utilizing a Physiea MCR 301 rheometer (Anton Paar, GmbH, Germany), equipped with a conical plate of 60 mm diameter (CP-60). To prevent water evaporation during the tests, the periphery of the samples was coated with a thin layer of liquid paraffin, and the setup was shielded with an anti-volatile cover for precision in measurements. The gelation monitoring process for s-0, s-0.2, s-0.4, and s-0.6 aqueous solutions involved employing an oscillatory mode set at a fixed frequency of 1 Hz, under a maintained temperature of 38 °C. The amplitude sweep tests were executed to determine the linear viscoelastic region (LVR) of the samples: pre-cured hydrogel-10, pre-cured hydrogel-15, and pre-cured hydrogel-20 (Fig. S1 in the electronic supplementary information, ESI). To further evaluate the thixotropic characteristics of these pre-cured hydrogels, three interval thixotropy tests (3ITT) were undertaken, employing an oscillatory mode set at a frequency of 1 Hz. During the stages of structural destruction and recovery, specific amplitudes were selected: a large amplitude of 500% lasting for 200 s and a small amplitude of 0.1% also enduring for the same period.

Morphological Observation of the Lyophilized Samples

The s-0 and s-0.2 aqueous solutions were subjected to heating at 38 °C for specified durations: 0, 3 and 6 h. This procedure induced the transformation of the solutions into diverse states: an aqueous solution, a weak hydrogel, and a printable pre-cured hydrogel respectively. To prepare lyophilized samples from these at different gelation stages for subsequent analysis, an initial step involved freezing the samples at −20 °C for a 24-h period. Subsequently, the samples were ripened in ethanol at −5 °C for an additional 24 h. Following this, the samples were thawed at room temperature, and the ethanol was replaced with deionized water, yielding the related lyophilized samples after lyophilization. The cross-sectional morphological characteristics of these lyophilized samples were analyzed using field emission scanning electron microscopy (FE-SEM, Hitachi S-4800, Japan) with gold spray for 60 s employing. These cross-sectional samples were obtained by being fractured in liquid nitrogen.

Productions of 3D-printed Hydrogel or Sponge

The 3D printing process for the pre-cured hydrogel-0.2 and pre-cured hydrogel-20 samples was conducted using a 3D bioprinter (Bio-Architect-WS, Regenovo, China). Initially, distinct aqueous mixtures were loaded into cartridges compatible with the 3D printer. A 38 °C water bath facilitated a 6-h heating period, resulting in the formation of the pre-cured hydrogels. After being heated, the cartridges containing the pre-cured hydrogels were installed into the 3D printer, and started to operate at room temperature. The printing parameters encompassed an air pressure between 0.2–0.25 MPa, a printing speed of 30

https://doi.org/10.1007/s10118-023-3059-3

mm/s, the use of a 0.4 mm needle, and an adjustable printing gap of 1–2 mm. Using a systematic, layer-by-layer process along the *Z*-axis, the printer adhered to a pre-determined model to create 3D-printed pre-cured hydrogel-0.2 and pre-cured hydrogel-20 samples, designated as Silk-0.2-hy and Silk-0-hy respectively. Subsequently, the Silk-0.2-hy sample underwent a 24-hour cooling process at −20 °C, followed by freeze-drying, culminating in a 3D-printed porous sponge labelled as Silk-0.2-sp.

ALP-induced Mineralization of 3D-printed Hydrogel or Sponge

A solution of triethanolamine buffer was prepared by dissolving 55 mL of triethanolamine into 2 L of deionized water. The pH of this solution was then meticulously adjusted to 9.5 using 1 mol/L of hydrochloric acid. Glycerol calcium phosphate was subsequently dissolved in the triethanolamine buffer solution at a concentration of 0.05 mol/L, yielding the mineralization solution, as per the method outlined in reference.[32] In the subsequent process, 3D-printed pre-cured hydrogels or 3D-printed sponges were introduced into the mineralization solution, maintaining a volume ratio of 1:10 between the sample and the solution. This setup was incubated at 37 °C in a light-shielded environment. The mineralization solution was refreshed every 12 h on the first day and every 24 h from the second day onward. The samples derived from Silk-0-hy after 0 and 7 days of mineralization were designated as Silk-0-d0-hy and Silk-0-d7-hy respectively. The samples produced from Silk-0.2-hy after 0, 1, 3, 5 and 7 days of mineralization were denoted as Silk-0.2-d0-hy, Silk-0.2-d1-hy, Silk-0.2-d3-hy, Silk-0.2-d5-hy, and Silk-0.2-d7-hy, respectively. Similarly, the samples resulting from Silk-0.2-sp after 0, 1, 3, 5, and 7 days of mineralization were termed as Silk-0.2-d0-sp, Silk-0.2-d1-sp, Silk-0.2-d3-sp, Silk-0.2-d5-sp, and Silk-0.2-d7-sp, respectively.

Characterizations

The cross-sectional morphologies of the 3D-printed RSF-mineral composite hydrogels or sponges undergoing various stages of mineralization using FESEM, which entailed a gold spray for 60 s. These cross-sectional samples were obtained through fracture by liquid nitrogen. To assess the composition, mineral content, crystalline form of the mineral, and the structure of the samples, a range of analytical measurements were employed. These included a thermogravimetric analyzer (Perkin Elemer Pyris 1), an X-ray diffraction analyzer (PANalytical X'Pert Pro X), and an infrared spectrometer (FTIR, Nicolet 6700, USA). Herein, the thermogravimetric analysis was conducted under air gas with a heating rate of 10 °C/min, ranging from 50 °C to 800 °C. The compressive properties of the 3D-printed RSF-mineral composite hydrogels and 3D-printed RSF-mineral composite sponges were evaluated using an Instron 5565 universal mechanics tester equipped with a 500 N sensor, at a compression rate of 1 mm/min. The samples for this test, with dimensions of 10 mm × 10 mm × 3 mm (length × width × thickness) and a printing gap of 1.5 mm, were measured four times each to ensure precision. The resulting data were subsequently averaged to provide a comprehensive and reliable representation of the mechanical properties.

Cell Viability

3D-printed RSF-mineral composites, including hydrogel and sponges, post-sterilization, were immersed in an incomplete medium (*α*-MEM, HyClone, USA) with the addition of 1% penicillin-streptomycin (HyClone, USA), yielding respective extracts after a 24-h incubation period. The rat bone marrow mesenchymal stem cells (rBMSCs) used in this study were isolated from Sprague Dawley (SD) rats, then cultured in complete medium comprising α-MEM, 10% heat-inactivated fetal bovine serum (FBS; Gibco, USA) and 1% penicillin/streptomycin. Subsequently, rBMSCs were seeded in a 96-well plate at a density of 5×10^3 cells per well. These cells were cultured in a DMEM medium, supplemented with 10% fetal bovine serum and 1% penicillin-streptomycin. This 96-well plate was then placed in an incubator maintained at 37 °C and 5% CO_2 for a duration of 24 h. Following this, the DMEM medium was substituted with the extracts derived from the 3D-printed RSF-mineral composites, and the incubation process was continued for an additional 24-h period. The cell counting kit-8 was employed to assess cell viability. The calculation of cell viability was based on the following equation:

$$\text{Cell viability}\,(\%) = \frac{[A]_{\text{test}} - [A]_{\text{blank}}}{[A]_{\text{control}} - [A]_{\text{blank}}} \times 100\% \quad (1)$$

Statistical Analysis

Origin Pro 2022 statistical software was used for statistical analysis. The results were expressed as mean ± SD. Unpaired T test was used to compare the differences among different groups. A p-value <0.05 (*) was considered as statistically significant and a p-value<0.001 (***) was considered as highly significant.

RESULTS AND DISCUSSION

Formation of the Pre-cured Hydrogels

Building on our group's previous research, it was revealed that an injectable hydrogel could be prepared upon heating RSF and HPC mixed aqueous solution with a solid content of 10 wt%.[33] In this section, with the assistance of HPC, attempts were made to develop the RSF pre-cured hydrogel of higher solid content and the ALP-involved RSF pre-cured hydrogels. As shown in Fig. 2(a), the RSF pre-cured hydrogels could be formed with or without the addition of ALP. However, the ALP in formulation delayed the formation of pre-cured hydrogels, shifting the sol-gel transition point to a later stage, and the delay was more pronounced as the ALP concentration increased. This resulted in the modulus of ALP-incorporated samples was lower when heating for the same duration.

Subsequently, our previous study also reported that RSF pre-cured hydrogel was RSF microhydrogels in essence.[34] Following this, it was recognized that RSF microhydrogels could undergo a transformation into RSF nanospheres through a freezing process. As a result, freezing and freeze-drying procedures yielded unique interior microstructures in the lyophilized sample from RSF pre-cured hydrogel, characterized by walls of stacked nanospheres.[35] To investigate the formation kinetics of RSF microhydrogel in this study, the observation of the interior microstructures was conducted for the lyophilized samples across various stages of gelation of the RSF pre-cured hydrogel (named as pre-cured hydrogel-20) and the ALP-involved RSF pre-cured hydrogel (named as pre-cured hydrogel-0.2). Fig. 2(b-i) portrays a dense and smooth inner wall of the samples lyophilized from the RSF and HPC mixed aqueous solution, which indicated the absence of microhydrogel formation in the mixture at initial

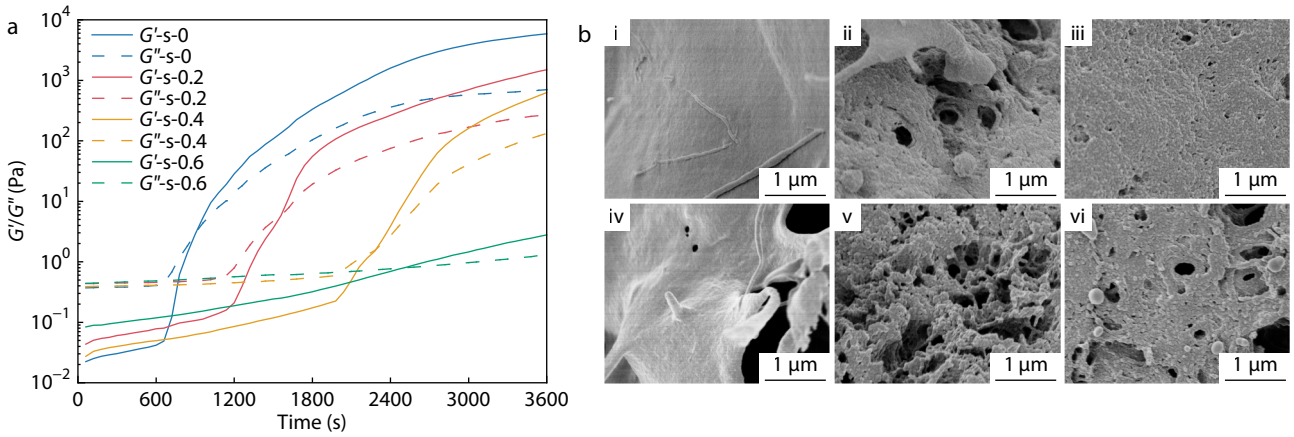

Fig. 2 (a) Evaluation of *G*' and *G*" in gelation process of ALP-involved RSF aqueous solution at 38 °C of varying ALP content; (b) Representative SEM images of the cross-section of the lyophilized samples from (i) s-0 and its corresponded hydrogel samples at different stages (ii and iii) or from (iv) s-0.2 and its corresponded hydrogel samples at different stages (v and vi).

state (aqueous solution). As the heating duration was extended, the interior microstructures of corresponding lyophilized samples of weak hydrogel and printable pre-cured hydrogel displayed a stack of nanospheres (Figs. 2b-ii and 2b-iii), signifying the progressive formation of microhydrogels within the RSF/HPC mixture under heating. Further examination was conducted for the mixture of RSF, HPC and ALP and similar observations were separately made in the samples lyophilized from RSF/HPC/ALP mixture at different stages of gelation (Figs. 2b-iv–2b-vi). The results implied that the formed ALP-involved RSF pre-cured hydrogel were also consisted of RSF microhydrogels while the addition of ALP did not significantly prevent the formation of RSF microhydrogels.

Thixotropic Properties of the Pre-cured Hydrogels

The RSF pre-cured hydrogels and the ALP-involved RSF pre-cured hydrogels were subjected to a three interval thixotropy test (3ITT), in which a small amplitude of 0.1% and a large amplitude of 500% was separately selected to observe the structural recovery and destruction of these pre-cured hydrogels. Fig. 3(a) presents the 3ITT results for the RSF pre-cured hydrogels of varied solid contents. Generally, during the initial phase of a small amplitude oscillatory shear (SAOS) measurement, it was revealed that the storage modulus (*G*') of the samples surpassed the loss modulus (*G*"), which was indicative of the hydrogels' rheological properties. The subsequent phase, a large amplitude oscillatory shear (LAOS) measurement, demonstrated a swift decline in *G*', which became smaller than *G*", thereby indicating fluid-like rheological behaviors. In the third SAOS phase, the samples' *G*' exhibited a rapid recovery, surpassing *G*" in a short time frame and once again displaying gel-like rheological behaviors. The rapid alternation between gel and fluid states under varying shear conditions signified the thixotropic characteristics of the RSF pre-cured hydrogels. Fig. S2 (in ESI) elucidates the variation in viscosity in relation to shear strain, corresponding to the 3ITT. This further substantiated the pre-cured hydrogels' thixotropic nature by revealing a swift decrease in viscosity under large amplitude and rapid recovery under small amplitude.

Subsequent trials were conducted to the ALP-involved RSF pre-cured hydrogels with various concentration of ALP in the formulation. Fig. 3(b) illustrates that all the ALP-involved RSF pre-cured hydrogels also demonstrated thixotropic properties, that is, fluid behavior when it is sheared while self-supporting after standing. Nevertheless, the modulus of ALP-incorporated samples was lower than that of ALP-free sam-

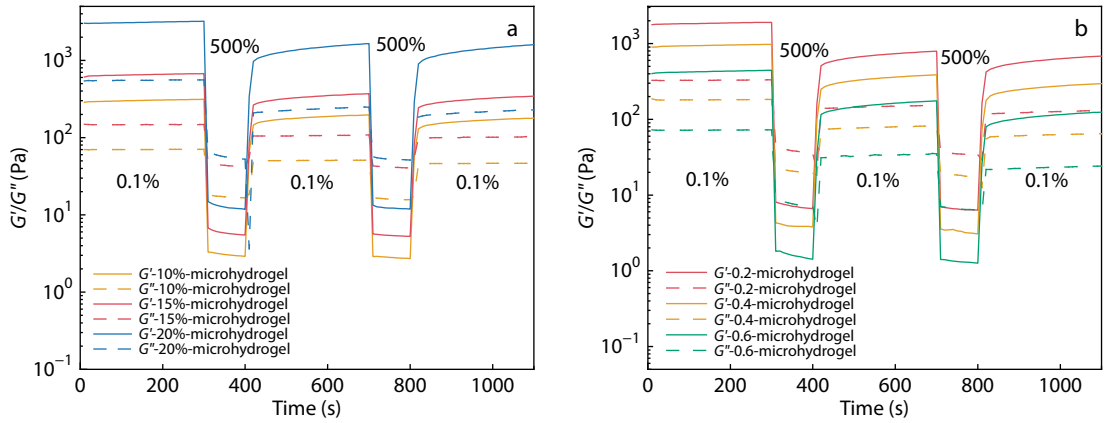

Fig. 3 Destruction-recovery tests of (a) RSF pre-cured hydrogels with varying solid contents and (b) ALP-involved RSF pre-cured hydrogels with varying ALP concentrations at 25 °C.

https://doi.org/10.1007/s10118-023-3059-3

ples. The reduction of modulus was more pronounced as the ALP concentration increased, which was because the delay of hydrogel formation was exacerbated as the ALP concentration increased.

It was reported that thixotropic properties of RSF pre-cured hydrogels largely stem from the presence of RSF microhydrogels, among which were composed of irreversibly β-sheet domains and numerous reversible interactions (*i.e.*, hydrophobic interaction, hydrogen bond interaction, static electronic interaction, and entanglements).[34] In the current study, we induced conformational transition of RSF chains using HPC upon heating to generate RSF microhydrogels. These microhydrogels demonstrated thixotropic properties, and the addition of ALP did not hinder the formation of RSF microhydrogels or eliminate their thixotropic properties although the modulus of ALP-incorporated samples decreased.

During the 3D printing process, constant pressure propels the sample towards the nozzle. As the cross-sectional area reduces, the applied shear rate on the sample drastically increases, leading to a decrease in modulus of the pre-cured hydrogel, thereby facilitating its egress from the nozzle. The removal of shear allows the modulus of the pre-cured hydrogel to promptly recover, thus exhibiting the self-supporting characteristics of the pre-cured hydrogel. The increase of modulus is approval of its enhanced self-supporting capabilities. This analysis informed our selection of the pre-cured hydrogel-20 sample and the pre-cured hydrogel-0.2 sample whose modulus were relatively higher, for application in extrusion-based 3D printing.

Printability of the Pre-cured Hydrogels

In order to scrutinize the performance of pre-cured hydrogels within the context of extrusion-based 3D printing, the pre-cured hydrogel-20 sample and the pre-cured hydrogel-0.2 sample were initially formed in cartridges. Subsequently, these cartridges were loaded onto a 3D-printer for the execution of the printing process at ambient temperature. Fig. 4 depicts the macro-morphology of both pre-cured hydrogels before and after being immersed in a mineralizing solution (Ca-GP buffer solution, pH=9.5). Observations revealed that both samples of pre-cured hydrogels were capable of preserving predetermined 3D structures after printing (Figs. 4a and 4b). Furthermore, it was noted that the structural stability could be maintained even being printed over 10 layers (height: 3 mm). Upon completion of a 7-days mineralization period, both 3D-printed pre-cured hydrogels retained their initial morphology and 3D structures (Figs. 4c–4f). The color of the sample with ALP involved transitioned to a milky white color (Figs. 4d and 4f), which was attributable to the generation of minerals within the ALP-involved RSF pre-hydrogel during the mineralization process.

Mineralization of the 3D-printed Hydrogel and Properties of the Composites Observation of Macro-Micro-Nano Morphologies

In a bid to determine whether the ALP-induced biomimetic mineralization method could generate homogeneous 3D-printed composites, cross-sectional morphologies of the hydrogels across different mineralization durations were analyzed at multiple scales (macro-micro-nanometer).

Macroscopically, as depicted in Fig. 5(a), the cross-sectional morphologies of the samples demonstrated no significant delamination or phase separation despite the increase in mineralization time. However, a gradual transition of sample color to milky white color was observed, indicative of the progressive formation and deposition of minerals within the 3D-printed hydrogels. The cross-sectional morphologies of the samples at the micron scale, as presented in Fig. 5(b) and Fig. S3 (in ESI), affirmed the homogeneous nature of the 3D-printed composite hydrogels. Observations at the nanoscale clearly evidenced the stepwise deposition of minerals within the hydrogels: at day 0 of mineralization, the interior wall of the lyophilized hydrogel appeared dense and smooth (Fig. S4 in ESI); as can been seen in Fig. 5(c), at the inception of mineralization at day 1, the mineral content was scant and sporadically distributed within the hydrogel; as the mineralization duration extended to 7 days, the deposited mineral content incrementally increased and displayed a relatively uniform distribution.

The aforementioned results suggested that ALP contained within the 3D-printed hydrogel could trigger enzymatic min-

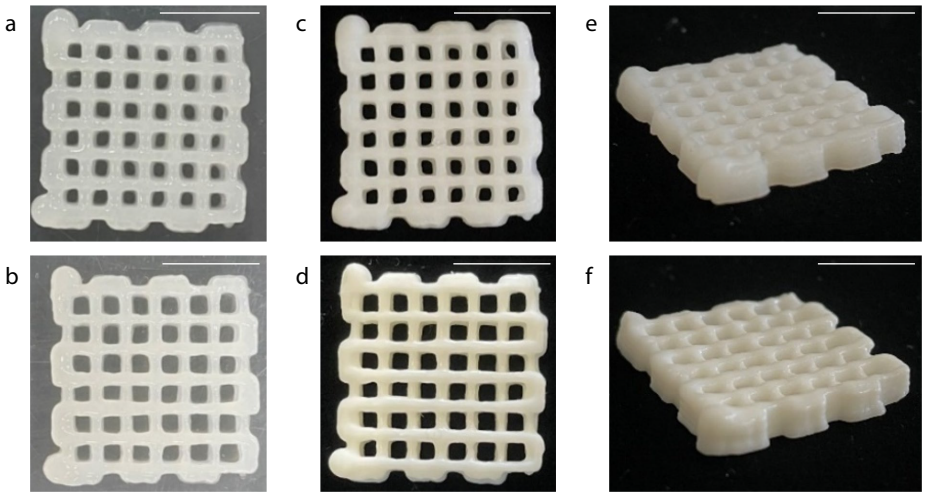

Fig. 4 Images of (a) Silk-0-hy and (b) Silk-0.2-hy before biomineralization. Images of (c, e) Silk-0-hy and (d, f) Silk-0.2-hy after biomineralization for 7 days. Size of the model is 2 cm × 2 cm × 3 mm. Scale bar: 1 cm.

https://doi.org/10.1007/s10118-023-3059-3

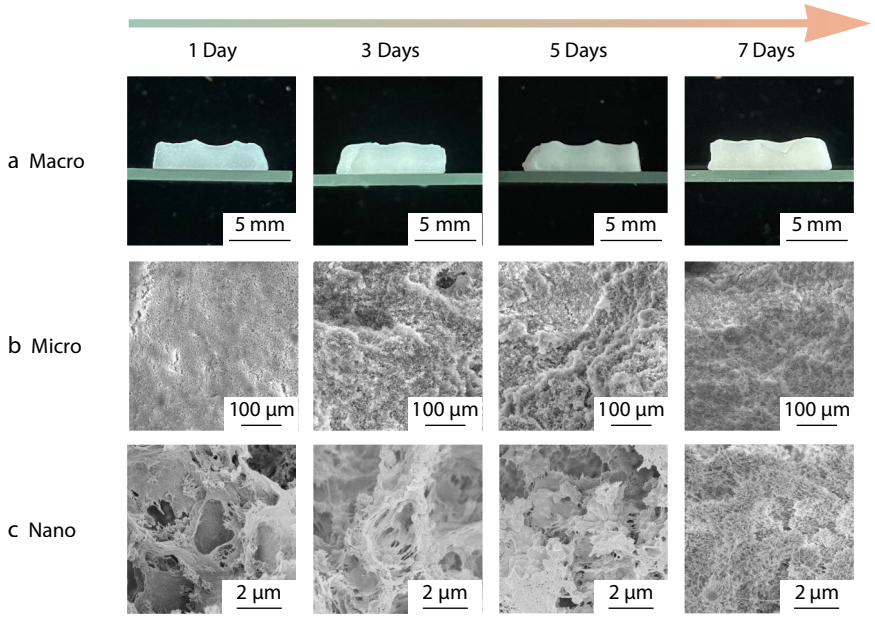

Fig. 5 Multi length-scale (a macro, b micro, c nano) morphological evolution of the 3D-printed ALP-involved pre-hydrogel derived from RSF during the 7-day observation period under ALP-induced mineralization.

eralization, facilitating the even deposition of minerals within the hydrogel, and obtaining a uniform 3D-printed composite hydrogel. During the mineralization process, the 3D-printed hydrogel, primarily composed of RSF, plays two pivotal roles: firstly, ALP complex to the RSF molecular chains, encapsulating the ALP due to complexation.[36] Secondly, the carboxyl groups on the RSF molecular chains could chelate the calcium ions in the mineralization solution and serve as a template for mineralization to modulate the biomimetic enzymatic mineralization reaction within the hydrogel.

Composition, Structure and Mechanical Properties

Following, the 3D-printed composite hydrogels, mineralized over varying durations, were characterized to assess their composition, structure and mechanical properties. TGA analysis (Fig. 6a) illustrated that, with increasing mineralization time, the 3D-printed composite hydrogel exhibited a progressive increment in mineralization deposition, specifically 19.0%, 27.5%, 35.2% and 40.0% after mineralization for 1, 3, 5 and 7 days respectively. In contrast, both the samples devoid of ALP and then subjected to 7 days of mineralization, and the samples enriched with ALP but unmineralized, demonstrated virtually no mineralization deposition. This suggested that the observed interior mineralization was resultant from the addition of ALP and that the quantity of deposited minerals escalated with extended mineralization duration, a conclusion congruent with the observations from the observation results of cross-sectional morphologies. This perspective was further corroborated by Fig. 6(b), where the corresponding XRD spectra of the 3D-printed composite hydrogel at day 0 of mineralization exhibited solely diffraction peaks ascribable to the β-sheet structure of RSF.[37] However, from the first day of mineralization, new diffraction peaks began to emerge at 25.9° and 31.8°, attributable to 002 and 211 crystallographic planes of HAP,[38] respectively. This indicated that the mineral species deposited within the hydrogel was indeed HAP. As the number of mineralization days further advanced, the content of HAP within the 3D-printed composite hydrogels proliferated, concomitant with a gradual increase in the intensity of its corresponding characteristic diffraction peaks.

To investigate the impact of HAP deposition on the conformational transition of RSF molecular chains, FTIR spectroscopy was employed to observe alterations in the secondary structures of the RSF molecular chains. These secondary structures predominantly bifurcate into two categories: the random coil of less crystalline and the β-sheet of more crystalline. The amide I bands of these structures are typically situated in the regions of 1650–1660 and 1620–1630 cm^{-1}, respectively, on the FTIR spectra.[39] Notably, ethanol treatment generally accelerates the transition of RSF molecular chains from random coil to β-sheet structure.[40] As illustrated in Fig. 6(c), prior to ethanol treatment, the RSF molecular chains of the 3D-printed composite hydrogels exhibited minimal conformational change with the extension of mineralization time, evidenced by the persistent presence of both random coil and β-sheet structures. Concurrently, the characteristic peak (1035 cm^{-1})[41] of HAP within the samples gradually intensified. Following ethanol maturation, the samples on the initial day of mineralization presented conspicuous absorbance of β-sheet structure. However, the intensity of these characteristic peak of β-sheet within the composite hydrogels diminished over extended mineralization time. This phenomenon could be attributed to the *in situ* deposition of HAP either impeding the conformational change of RSF molecular chains or disrupting the regularity of the β-sheet structure.

Figs. 6(e) and 6(f) separately depict the compressive modulus and representative compressive stress-strain curves of the 3D-printed composite hydrogels. They demonstrated the comparable compressive modulus of the silk-0.2-d0-hy and silk-0-d0-hy samples. This implied that the addition of ALP may hinder the formation of RSF pre-cured hydrogels but did

https://doi.org/10.1007/s10118-023-3059-3

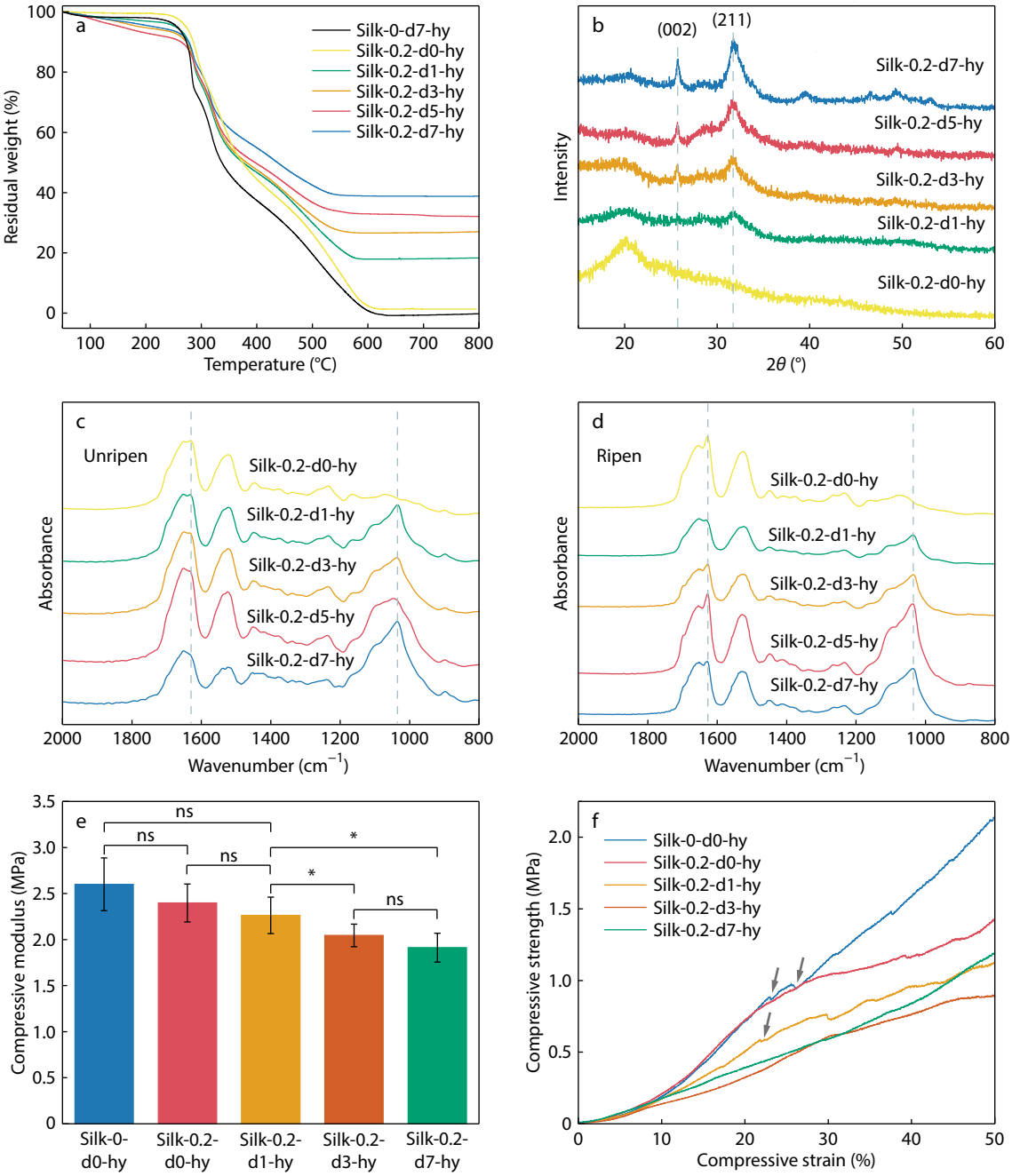

Fig. 6 (a) TGA curves and (b) XRD patterns of the samples; FTIR spectra of (c) unripened and (d) ripened samples; (e) Compressive modulus and (f) representative stress-strain curves of the silk-0-d0-hy, silk-0.2-d0-hy, silk-0.2-d1-hy, silk-0.2-d3-hy and silk-0.2-d7-hy samples. The arrows point out the first failure of the samples. $^{*}p<0.05$; ns: no significance; $n=4$.

not affect the mechanical strength of the ethanol-ripened composite hydrogels. In contrast, the compressive modulus of the 3D-printed composite hydrogel gradually decreases with an increase in mineralization duration. This decrease can be attributed to the partial degradation of silk protein molecular chains due to prolonged immersion in the highly alkaline mineralization solution, along with the deposition of HAP. The presence of HAP may hinder the conformational change of the RSF molecular chains into β-sheet structures, which are primarily responsible for the high-strength mechanical properties of RSF materials. Nevertheless, the 3D-printed composite hydrogels still exhibited a significant compressive modulus, ranging from 1.8 MPa to 2.5 MPa. This could be primarily attributed to the high solid content (approximately 20 wt%) of the hydrogels.

Mineralization of the 3D-printed Sponge and Properties of the Composites

Given that the occurrence of *in situ* mineralization is principally contingent on the diffusion of the mineralization solution into the matrix material, the rate of this process is intimately associated with the porous structure of the matrix material. Therefore,

https://doi.org/10.1007/s10118-023-3059-3

attempts were made to augment the mineralization rate of the 3D-printed hydrogel by putting the Silk-0.2-hy sample to a −20 ℃ environment for 24 h and subsequently being lyophilized, yielding 3D-printed porous sponges, Silk-0.2-sp.

The cross-sectional morphologies of the 3D-printed porous sponges following 0, 1, 3, 5 and 7 days of mineralization was depicted in Fig. 7(a). Notably, the samples on the initial day 0 of mineralization exhibited a porous structure, which was attributed to ice crystal growth, while the interior walls of the samples remained dense and smooth, characteristic of the morphology of porous sponge post freeze-drying of RSF hydrogel. As mineralization time was extended, HAP progressively accumulated within the samples. The thermogravimetric analysis (Fig. 7b) further showed that the HAP contents in the 3D-printed composite sponges on day 1, 3, 5 and 7 of mineralization was 25.7%, 34.5%, 37.2% and 45.2%, respectively. Although the mineral content gradually increases as mineralization time prolongs, it could be seen that a significantly smaller change in residual mass after 7 days of mineralization compared to the initial day. This may be attributed to the increasingly limited space for continuing mineral deposition and the diminished activity of ALP as time extends. Comparative analysis with the 3D-printed hydrogel after mineralization revealed a greater deposition of HAP within the 3D-printed composite sponges compared to the 3D-printed composite hydrogels over the same mineralization duration. This result is mainly because the porous structure in the 3D-printed sponge provided more space for HAP deposition.

Compression tests conducted on the mineralized 3D-printed porous sponges in a wet state indicated that (Figs. 7c and 7d), the trends of the compression modulus of the 3D-printed RSF-mineral composite sponges across different mineralization periods were essentially consistent with those of the 3D-printed RSF-mineral composite hydrogel. For instance, the compression modulus of the silk-0-d0-sp and silk-0.2-d0-sp samples were comparable, but observed a slight decrease with an increase in the number of mineralization days. Generally, the compressive modulus of the composite sponges could be modulated between 0.8–1.8 MPa. The representative stress-strain curves of the 3D-printed RSF-mineral composite sponges further revealed that the material also possessed significant toughness, with samples not fracturing even after being compressed to 50%.

In previous literatures,[42,43] the compressive modulus of both the human articular cartilages and bone has been reported to vary within the megapascal grade. Therefore, it was expected that these 3D-printed RSF-mineral composites, including hydrogels and sponges, might be applied in the short-term replacement of various human bone tissue (*i.e.*, articular cartilages, subchondral bone, bone) according to their mechanical properties, mineral content and designed architectures.

Cytotoxicity of the 3D-printed Composite Hydrogels and the 3D-printed Composite Sponges

The good biocompatibility of the RSF-based material produced by various ways has been widely reported in the literatures.[44–46] For instance, it was noted that the 3D-printed RSF material demonstrated good cytocompatibility for human mesenchymal stem cells (hMSCs).[34] Moreover, the RSF-based materials with HAP doping could promote osteoblastic differentiation for bone marrow mesenchymal stem cells (BMSCs).[22,47,48]

To confirm that our 3D-printed composite hydrogels and sponges also have the potential of supporting cell growth and proliferation, BMSCs were co-cultured with the extracts of the 3D-printed RSF-mineral hydrogels and the 3D-printed RSF-mineral sponges with different mineralization durations. As shown in Figs. 8(a) and 8(b), the rBMSCs cell viability of two kinds of 3D-printed RSF-mineral composites remained above 90%. The results indicated that the obtained 3D-printed RSF-mineral composites exhibited non-cytotoxicity and there was

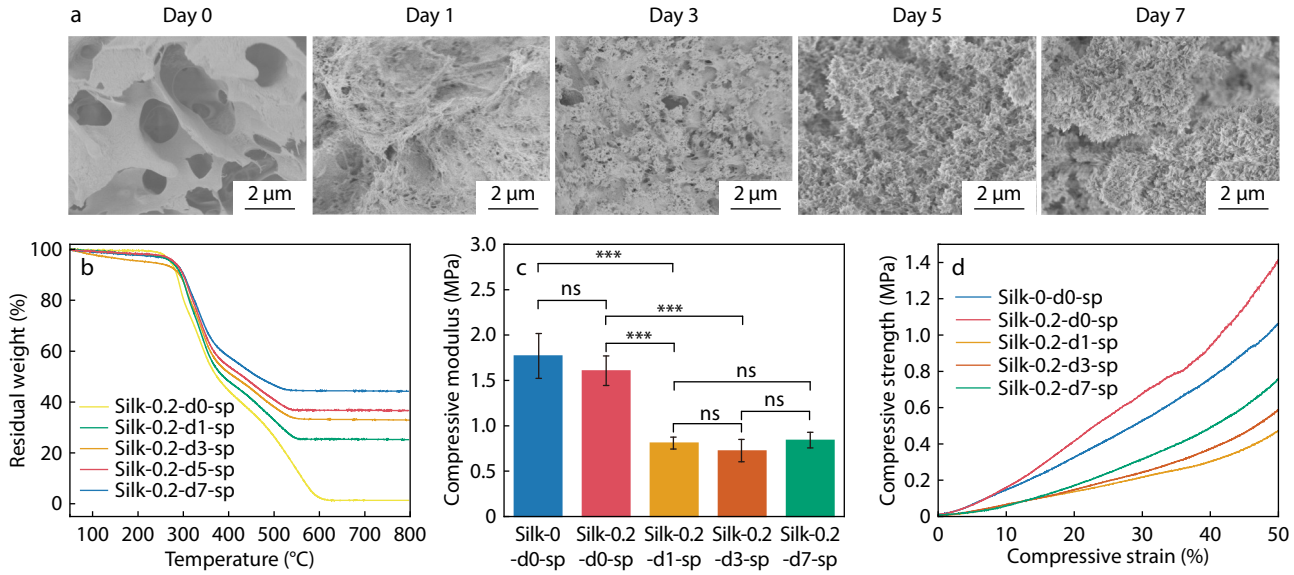

Fig. 7 (a) Representative SEM images and (b) TGA curves of Silk-0.2-d0-sp, Silk-0.2-d1-sp, Silk-0.2-d3-sp, Silk-0.2-d5-sp and Silk-0.2-d7-sp; (c) Compressive modulus and (d) Representative stress-strain curves of the silk-0-d0-sp, silk-0.2-d0-sp, silk-0.2-d1-sp, silk-0.2-d3-sp and silk-0.2-d7-sp samples. $^{***}p<0.001$; ns: no significance; $n=4$.

https://doi.org/10.1007/s10118-023-3059-3

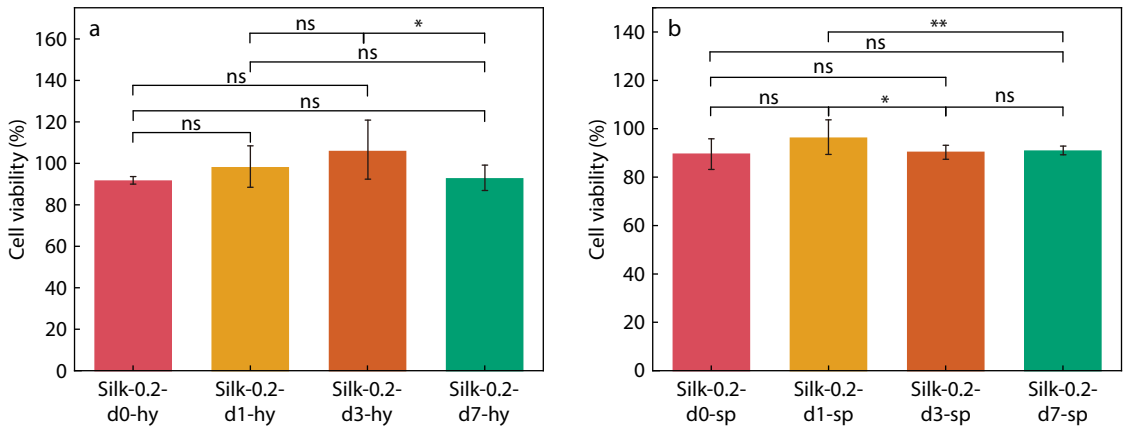

Fig. 8 Cytotoxicity tests of extracts from varied (a) 3D-printed RSF-mineral composite hydrogels and (b) 3D-printed RSF-mineral composite sponges by cell counting kit-8. $^{*}p<0.05$; $^{**}p<0.01$; ns: no significance; $n=6$.

no apparent correlation between the content of HA and the cytotoxicity of the 3D-printed RSF-mineral composites. It has also been researched a lot that the RSF-HAP composite materials have good cytocompatibility and supporting cell differentiation.[48–50] In our present work, we developed a novel method to prepare the RSF-HAP composite material and the composition of this composite material has not changed. Therefore, we infer that our 3D-printed RSF-HAP composites has good cytocompatibility and support osteogenic differentiation of BMSCs as well. Considering that the HAP content in the nature compact bone is about 65% according to previous research,[51] this newly-developed 3D-printed RSF-mineral hydrogels and 3D-printed RSF-mineral sponges are one step closer to the constituent of the innate tissue based on the premise of satisfactory biocompatibility.

CONCLUSIONS

In this study, ALP-involved RSF pre-cured hydrogel with both thixotropic properties and extrudable 3D-printing performance were prepared by a straightforward method of heating RSF, HPC, and ALP mixture. Rheological tests and observation of microscopic morphology of lyophilized samples at various gelation stages together revealed that this pre-cured hydrogel was essentially composed of RSF microhydrogels, which contributed to its thixotropic properties. The addition of HPC accelerated the formation of these microhydrogels upon heating. The ALP, which was encapsulated within the 3D-printed hydrogel or 3D-printed sponge, initiated a biomimetic enzyme-induced mineralization by utilizing RSF chains as templates when immersing these 3D-printed materials in Ca-GP mineralizing solution. This reaction enabled the production of even 3D-printed RSF-mineral composites, including hydrogels and sponges, with adjustable mechanical properties within megapascal grade and variable hydroxyapatite content. By combining 3D printing technology with biomimetic enzymatic mineralization, this system overcame the limitation of surface-only mineralization in the composites, resulting in materials with a more even and intricate structure. Additionally, the obtained 3D-printed RSF-mineral composites were proven to be non-cytotoxic for rBMSCs, making them promising for applications in tissue replacement where osteoinduction and complex structures are desired.

Conflict of Interests

Zheng-Zhong Shao is an editorial board member for *Chinese Journal of Polymer Science* and was not involved in the editorial review or the decision to publish this article. All authors declare that there are no competing interests.

Electronic Supplementary Information

Electronic supplementary information (ESI) is available free of charge in the online version of this article at http://doi.org/10.1007/s10118-023-3059-3.

ACKNOWLEDGMENTS

This work was financially supported by the National Nature Science Foundation of China (No. 21935002). We also sincerely thank Gao Han (Ph.D candidate) at Fudan University for his support in cell experiment.

REFERENCES

1 Chen, H.; Liu, Y.; Wang, C.; Zhang, A.; Chen, B.; Han, Q.; Wang, J. Design and properties of biomimetic irregular scaffolds for bone tissue engineering. *Comput. Biol. Med.* **2021**, *130*, 104241.
2 Zhang, M.; Matinlinna, J. P.; Tsoi, J. K. H.; Liu, W.; Cui, X.; Lu, W. W.; Pan, H. Recent developments in biomaterials for long-bone segmental defect reconstruction: a narrative overview. *J. Orthop. Translat.* **2020**, *22*, 26–33.
3 Liu, Y. H.; Liu, W.; Zheng, Z. L.; Wei, X.; Shah, N. A.; Lin, H.; Zhao, B. S.; Huang, S. S.; Xu, J. Z.; Li, Z. M. Fabrication of highly anisotropic and interconnected porous scaffolds to promote preosteoblast proliferation for bone tissue engineering. *Chinese J. Polym. Sci.* **2021**, *39*, 1191–1199.
4 Neovius, E.; Engstrand, T. Craniofacial reconstruction with bone and biomaterials: review over the last 11 years. *J. Plast. Reconstr. Aesthet. Surg.* **2010**, *63*, 1615–1623.
5 Lauthe, O.; Soubeyrand, M.; Babinet, A.; Dumaine, V.; Anract, P.; Biau, D. J. The indications and donor-site morbidity of tibial cortical strut autografts in the management of defects in long bones. *Bone Joint J.* **2018**, *100-B*, 67–674.
6 Han, J.; Wu, J.; Xiang, X.; Xie, L.; Chen, R.; Li, L.; Ma, K.; Sun, Q.; Yang, R.; Huang, T.; Tong, L.; Zhu, L.; Wang, H.; Wen, C.; Zhao, Y.;

Wang, J. Biodegradable BBG/PCL composite scaffolds fabricated by selective laser sintering for directed regeneration of critical-sized bone defects. *Mater. Des.* **2023**, *225*, 111543.
7 Stevens, M. M. Biomaterials for bone tissue engineering. *Mater. Today* **2008**, *11*, 18–25.
8 Kumar, A.; Kargozar, S.; Baino, F.; Han, S. S. Additive manufacturing methods for producing hydroxyapatite and hydroxyapatite-based composite scaffolds: a review. *Front. Mater.* **2019**, *6*, 313.
9 Ehret, C.; Aid, R.; Dos Santos, B. P.; Rey, S.; Letourneur, D.; Amedee Vilamitjana, J.; de Mones, E. Bone regeneration in small and large segmental bone defect models after radiotherapy using injectable polymer-based biodegradable materials containing strontium-doped hydroxyapatite particles. *Int. J. Mol. Sci.* **2023**, *24*, 5429.
10 Hu, J.; Cai, X.; Mo, S. B.; Chen, L.; Shen, X. Y.; Tong, H. Fabrication and characterization of chitosan-silk fibroin/hydroxyapatite composites *via in situ* precipitation for bone tissue engineering. *Chinese J. Polym. Sci.* **2015**, *33*, 1661–1671.
11 Zhou, H.; Lee, J. Nanoscale hydroxyapatite particles for bone tissue engineering. *Acta Biomater.* **2011**, *7*, 2769–2781.
12 Ma, P. X. Biomimetic materials for tissue engineering. *Adv. Drug Deliv. Rev.* **2008**, *60*, 184–198.
13 Trakoolwannachai, V.; Kheolamai, P.; Ummartyotin, S. Characterization of hydroxyapatite from eggshell waste and polycaprolactone (PCL) composite for scaffold material. *Compos. B Eng.* **2019**, *173*, 106974.
14 Yan, H.; Wang, Z.; Li, L.; Shi, X.; Jia, E.; Ji, Q.; Wang, Y.; Ito, Y.; Wei, Y.; Zhang, P. DOPA-derived electroactive copolymer and IGF-1 immobilized poly(lactic-*co*-glycolic acid)/hydroxyapatite biodegradable microspheres for synergistic bone repair. *Chem. Eng. J.* **2021**, *416*, 129129.
15 Abouzeid, R. E.; Khiari, R.; Salama, A.; Diab, M.; Beneventi, D.; Dufresne, A. In situ mineralization of nano-hydroxyapatite on bifunctional cellulose nanofiber/polyvinyl alcohol/sodium alginate hydrogel using 3D printing. *Int. J. Biol. Macromol.* **2020**, *160*, 538–547.
16 Chen, P.; Liu, L.; Pan, J.; Mei, J.; Li, C.; Zheng, Y. Biomimetic composite scaffold of hydroxyapatite/gelatin-chitosan core-shell nanofibers for bone tissue engineering. *Mater. Sci. Eng. C Mater. Biol. Appl.* **2019**, *97*, 325–335.
17 Kaushik, S.; Thungon, P. D.; Goswami, P. Silk fibroin: an emerging biocompatible material for application of enzymes and whole cells in bioelectronics and bioanalytical sciences. *ACS Biomater. Sci. Eng.* **2020**, *6*, 4337–4355.
18 Fang, G.; Huang, Y.; Tang, Y.; Qi, Z.; Yao, J.; Shao, Z.; Chen, X. Insights into silk formation process: correlation of mechanical properties and structural evolution during artificial spinning of silk fibers. *ACS Biomater. Sci. Eng.* **2016**, *2*, 1992–2000.
19 Yang, G.; Gu, K.; Shao, Z. The investigation from animal silks to silk protein-based materials. *Acta Polymerica Sinica* (in Chinese) **2021**, *52*,16–28.
20 Kim, H.; Che, L.; Ha, Y.; Ryu, W. Mechanically-reinforced electrospun composite silk fibroin nanofibers containing hydroxyapatite nanoparticles. *Mater. Sci. Eng. C Mater. Biol. Appl.* **2014**, *40*, 324–335.
21 Mi, R.; Liu, Y.; Chen, X.; Shao, Z. Structure and properties of various hybrids fabricated by silk nanofibrils and nanohydroxyapatite. *Nanoscale* **2016**, *8*, 20096–20102.
22 Yan, Z.; Chen, W.; Jin, W.; Sun, Y.; Cai, J.; Gu, K.; Mi, R.; Chen, N.; Chen, S.; Shao, Z. An interference screw made using a silk fibroin-based bulk material with high content of hydroxyapatite for anterior cruciate ligament reconstruction in a rabbit model. *J. Mater. Chem. B* **2021**, *9*, 5352–5364.
23 Liu, X.; Yuk, H.; Lin, S.; Parada, G. A.; Tang, T. C.; Tham, E.; de la Fuente-Nunez, C.; Lu, T. K.; Zhao, X. 3D printing of living responsive materials and devices. *Adv. Mater.* **2018**, *30*, 1704821.
24 Xin, A.; Su, Y.; Feng, S.; Yan, M.; Yu, K.; Feng, Z.; Hoon Lee, K.; Sun, L.; Wang, Q. Growing living composites with ordered microstructures and exceptional mechanical properties. *Adv. Mater.* **2021**, *33*, e2006946.
25 Heveran, C. M.; Williams, S. L.; Qiu, J.; Artier, J.; Hubler, M. H.; Cook, S. M.; Cameron, J. C.; Srubar, W. V. Biomineralization and successive regeneration of engineered living building materials. *Matter* **2020**, *2*, 481–494.
26 Hoffmann, C.; Zollfrank, C.; Ziegler, G. Enzyme-catalysed synthesis of calcium phosphates. *J. Mater. Sci. Mater. Med.* **2008**, *19*, 907–915.
27 Rauner, N.; Meuris, M.; Zoric, M.; Tiller, J. C. Enzymatic mineralization generates ultrastiff and tough hydrogels with tunable mechanics. *Nature* **2017**, *543*, 407–410.
28 Douglas, T. E.; Messersmith, P. B.; Chasan, S.; Mikos, A. G.; de Mulder, E. L.; Dickson, G.; Schaubroeck, D.; Balcaen, L.; Vanhaecke, F.; Dubruel, P.; Jasen, A. J.; Leeuwenburgh, S. C. G. Enzymatic mineralization of hydrogels for bone tissue engineering by incorporation of alkaline phosphatase. *Macromol. Biosci.* **2012**, *12*, 1077–1089.
29 Yao, R.; Zhang, B.; Gao, T.; Zhang, N.; Wang, Y.; Meng, G.; He, J.; Wu, F. Dopamine enhances the mechanical and biological properties of enzyme-induced mineralized hydrogels. *J. Mater. Chem. B* **2020**, *8*, 9052–9061.
30 Bose, S.; Vahabzadeh, S.; Bandyopadhyay, A. Bone tissue engineering using 3D printing. *Mater. Today* **2013**, *16*, 496–504.
31 Gong, Z.; Huang, L.; Yang, Y.; Chen, X.; Shao, Z. Two distinct beta-sheet fibrils from silk protein. *Chem. Commun*. **2009**, 7506–7508.
32 Chen, G.; Liang, X.; Zhang, P.; Lin, S.; Cai, C.; Yu, Z.; Liu, J. Bioinspired 3D printing of functional materials by harnessing enzyme-induced biomineralization. *Adv. Funct. Mater.* **2022**, *32*, 2113262.
33 Gong, Z.; Yang, Y.; Ren, Q.; Chen, X.; Shao, Z. Injectable thixotropic hydrogel comprising regenerated silk fibroin and hydroxypropylcellulose. *Soft Matter* **2012**, *8*, 2875–2883.
34 Dong, T.; Mi, R.; Wu, M.; Zhong, N.; Zhao, X.; Chen, X.; Shao, Z. The regenerated silk fibroin hydrogel with designed architecture bioprinted by its microhydrogel. *J. Mater. Chem. B* **2019**, *7*, 4328–4337.
35 Chen, N.; Zhang, X.; Lyu, J.; Zhao, G.; Gu, K.; Xia, J.; Chen, Z.; Shao, Z. Preparation of a novel regenerated silk fibroin-based hydrogel for extrusion bioprinting. *Soft Matter* **2022**, *18*, 7360–7368.
36 Samal, S. K.; Dash, M.; Declercq, H. A.; Gheysens, T.; Dendooven, J.; Van Der Voort, P.; Cornelissen, R.; Dubruel, P.; Kaplan, D. L. Enzymatic mineralization of silk scaffolds. *Macromol. Biosci.* **2014**, *14*, 991–1003.
37 Su, D.; Yao, M.; Liu, J.; Zhong, Y.; Chen, X.; Shao, Z. Enhancing Mechanical Properties of Silk Fibroin Hydrogel through Restricting the Growth of beta-Sheet Domains. *ACS Appl. Mater. Interfaces* **2017**, *9*, 17489–17498.
38 Rapacz-Kmita, A.; Paluszkiewicz, C.; Ślósarczyk, A.; Paszkiewicz, Z. FTIR and XRD investigations on the thermal stability of hydroxyapatite during hot pressing and pressureless sintering processes. *J. Mol. Struct*. **2005**, *744–747*, 653–656.
39 Chen, X.; Shao, Z.; Marinkovic, N. S.; Miller, L. M.; Zhou, P.; Chance, M. R. Conformation transition kinetics of regenerated *Bombyx* mori silk fibroin membrane monitored by time-resolved FTIR spectroscopy. *Biophys. Chem.* **2001**, *89*, 25–34.
40 Li, Z.; Zheng, Z.; Yang, Y.; Fang, G.; Yao, J.; Shao, Z.; Chen, X. Robust protein hydrogels from silkworm silk. *ACS Sustainable Chem. Eng.* **2016**, *4*, 1500–1506.
41 Rehman, I.; Bonfield, W. Characterization of hydroxyapatite and carbonated apatite by photo acoustic FTIR spectroscopy. *J.*

Mater. Sci. Mater. Med. **1997**, *8*, 1–4.
42 Shepherd, D. E.; Seedhom, B. B. The 'instantaneous' compressive modulus of human articular cartilage in joints of the lower limb. *Rheumatology* **1999**, *38*, 124–132.
43 Gao, F.; Xu, Z.; Liang, Q.; Li, H.; Peng, L.; Wu, M.; Zhao, X.; Cui, X.; Ruan, C.; Liu, W. Osteochondral regeneration with 3D-printed biodegradable high-strength supramolecular polymer reinforced-gelatin hydrogel scaffolds. *Adv. Sci.* **2019**, *6*, 1900867.
44 Lujerdean, C.; Baci, G. M.; Cucu, A. A.; Dezmirean, D. S. The contribution of silk fibroin in biomedical engineering. *Insects* **2022**, *13*, 286.
45 Holland, C.; Numata, K.; Rnjak-Kovacina, J.; Seib, F. P. The biomedical use of silk: past, present, future. *Adv. Healthc. Mater.* **2019**, *8*, e1800465.
46 Da, G.; Ma, Y.; Lin, Q.; Shao, Z. Regenerated silk fibroin hydrogel with laponite/polydopamine composite nanoparticles. *Acta Polymerica Sinica* (in Chinese) **2023**, *54*, 95–105.
47 Chen, L.; Sun, L.; Liu, W.; Yao, J.; Shao, Z.; Zhao, B.; Chen, X. Long-lasting thixotropic natural polymeric hydrogel based on silk nanofibrils. *ACS Biomater. Sci. Eng.* **2023**, *9*, 4168–4177.
48 Saleem, M.; Rasheed, S.; Yougen, C. Silk fibroin/hydroxyapatite scaffold: a highly compatible material for bone regeneration. *Sci. Technol. Adv. Mater.* **2020**, *21*, 242–266.
49 Bharadwaz, A.; Jayasuriya, A. C. Recent trends in the application of widely used natural and synthetic polymer nanocomposites in bone tissue regeneration. *Mater. Sci. Eng. C Mater. Biol. Appl.* **2020**, *110*, 110698.
50 Zhang, H.; You, R.; Yan, K.; Lu, Z.; Fan, Q.; Li, X.; Wang, D. Silk as templates for hydroxyapatite biomineralization: a comparative study of *Bombyx mori* and *Antheraea pernyi* silkworm silks. *Int. J. Biol. Macromol.* **2020**, *164*, 2842–2850.
51 Sotome, S.; Uemura, T.; Kikuchi, M.; Chen, J.; Itoh, S.; Tanaka, J.; Tateishi, T.; Shinomiya, K. Synthesis and *in vivo* evaluation of a novel hydroxyapatite/collagen-alginate as a bone filler and a drug delivery carrier of bone morphogenetic protein. *Mater. Sci. Eng. C.* **2004**, *24*, 341–347.

https://doi.org/10.1007/s10118-023-3059-3